



<https://doi.org/10.1038/s41534-024-00820-1>

Non-symmetric Pauli spin blockade in a silicon double quantum dot

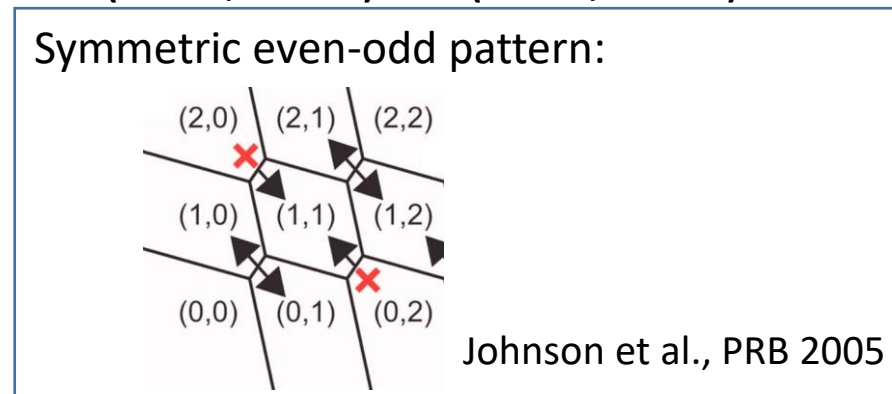
 Check for updates

Theodor Lundberg^{1,2}, David J. Ibberson^{2,3,4,9}, Jing Li^{5,6}, Louis Hutin⁶, José C. Abadillo-Uriel⁵, Michele Filippone⁵, Benoit Bertrand⁶, Andreas Nunnenkamp⁷, Chang-Min Lee⁸, Nadia Stelmashenko⁸, Jason W. A. Robinson⁸, Maud Vinet⁶, Lisa Ibberson², Yann-Michel Niquet⁵ & M. Fernando Gonzalez-Zalba⁹ ✉

¹Cavendish Laboratory, University of Cambridge, J.J. Thomson Avenue, Cambridge CB3 0HE, UK. ²Hitachi Cambridge Laboratory, J.J. Thomson Avenue, Cambridge CB3 0HE, UK. ³Quantum Engineering Technology Labs, University of Bristol, Tyndall Avenue, Bristol BS8 1FD, UK. ⁴Quantum Engineering Centre for Doctoral Training, University of Bristol, Tyndall Avenue, Bristol BS8 1FD, UK. ⁵Université Grenoble Alpes, CEA, IRIG, MEM/L_Sim, 38000 Grenoble, France. ⁶Université Grenoble Alpes, CEA, LETI, 38000 Grenoble, France. ⁷Faculty of Physics, University of Vienna, Boltzmanngasse 5, 1090 Vienna, Austria. ⁸Department of Materials Science and Metallurgy, University of Cambridge, 27 Charles Babbage Road, Cambridge CB3 0FS, UK. ⁹Present address: Quantum Motion, 9 Sterling Way, London N7 9HJ, UK. ✉e-mail: fernando@quantummotion.tech

Journal Club, 24.05.2024

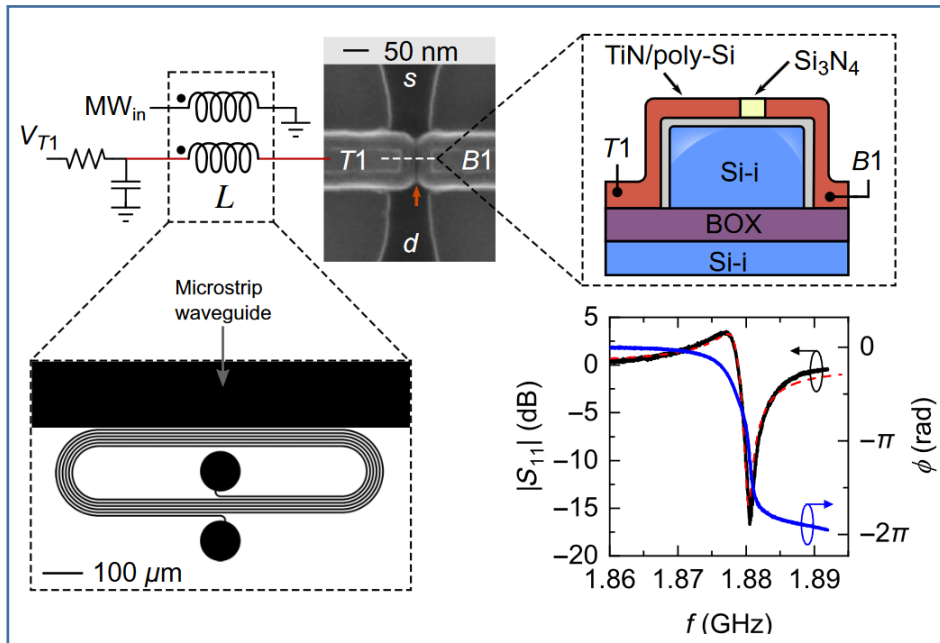
- Gate-dispersive sensing of electron QDs in Si nanowires (LETI devices)
- One manifestation of PSB in dispersive sensing: Interdot transition vanishes when B is increased
- Observation of *non-symmetric* PSB: either in the $(N+1, M-1)$ or $(N-1, M+1)$ state but not both for a given (N, M)



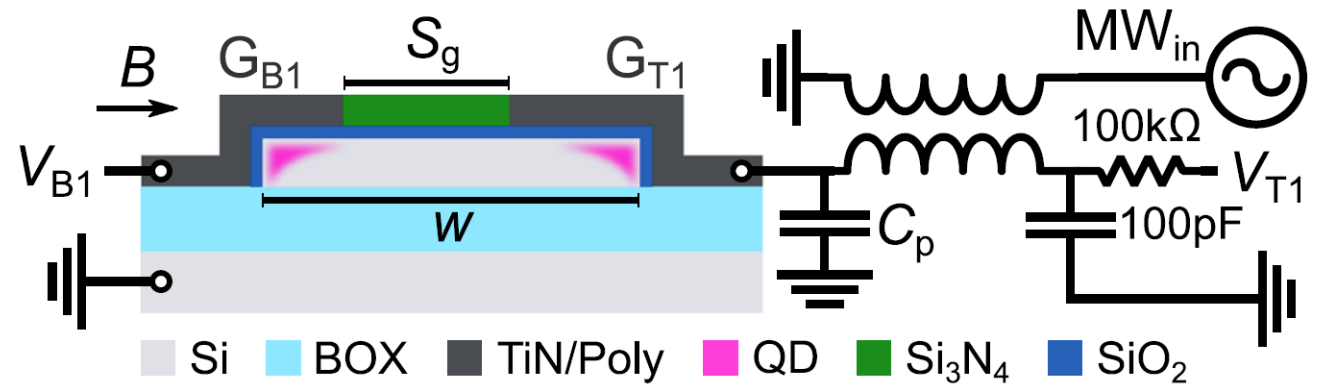
- Analysis in circuit QED framework identifies large spin-flip tunnel couplings for transitions with lifted PSB

Device & setup

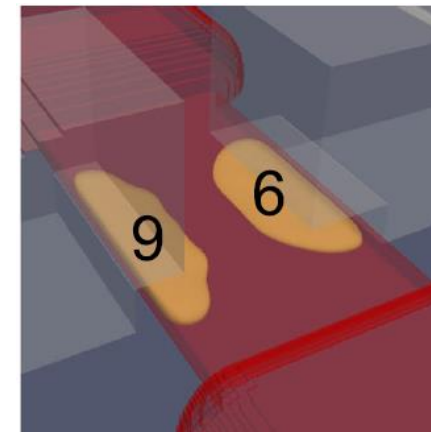
- Split-gate nanowire field-effect transistor
- Resonant circuit: superconducting NbN planar spiral inductor
- Inductively coupled to microstrip waveguide



Ibberson et al., PRX Quantum 2021

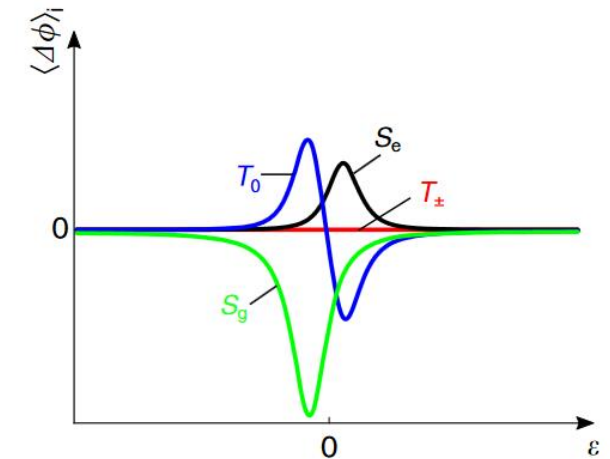
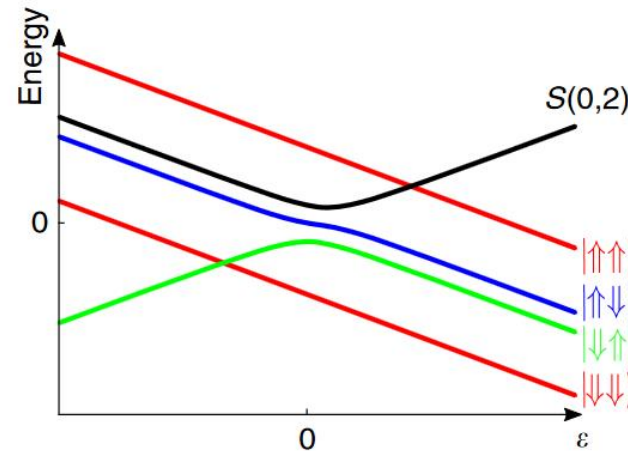
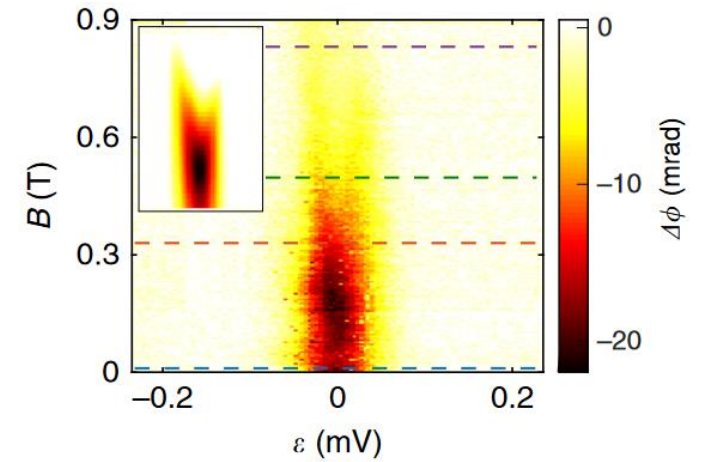
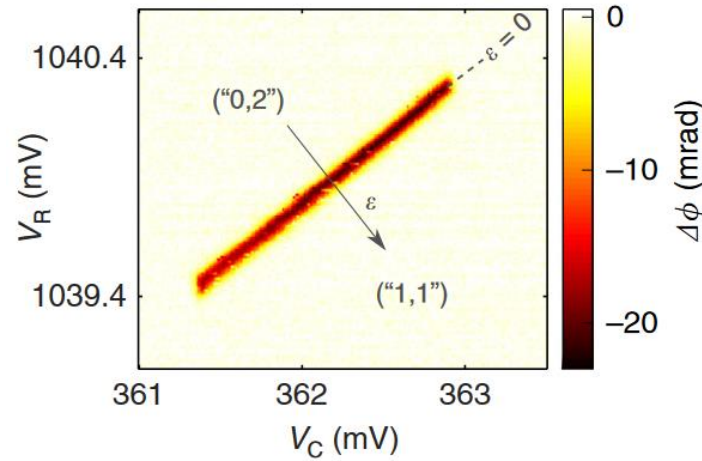


Simulation of electron density: corner QDs



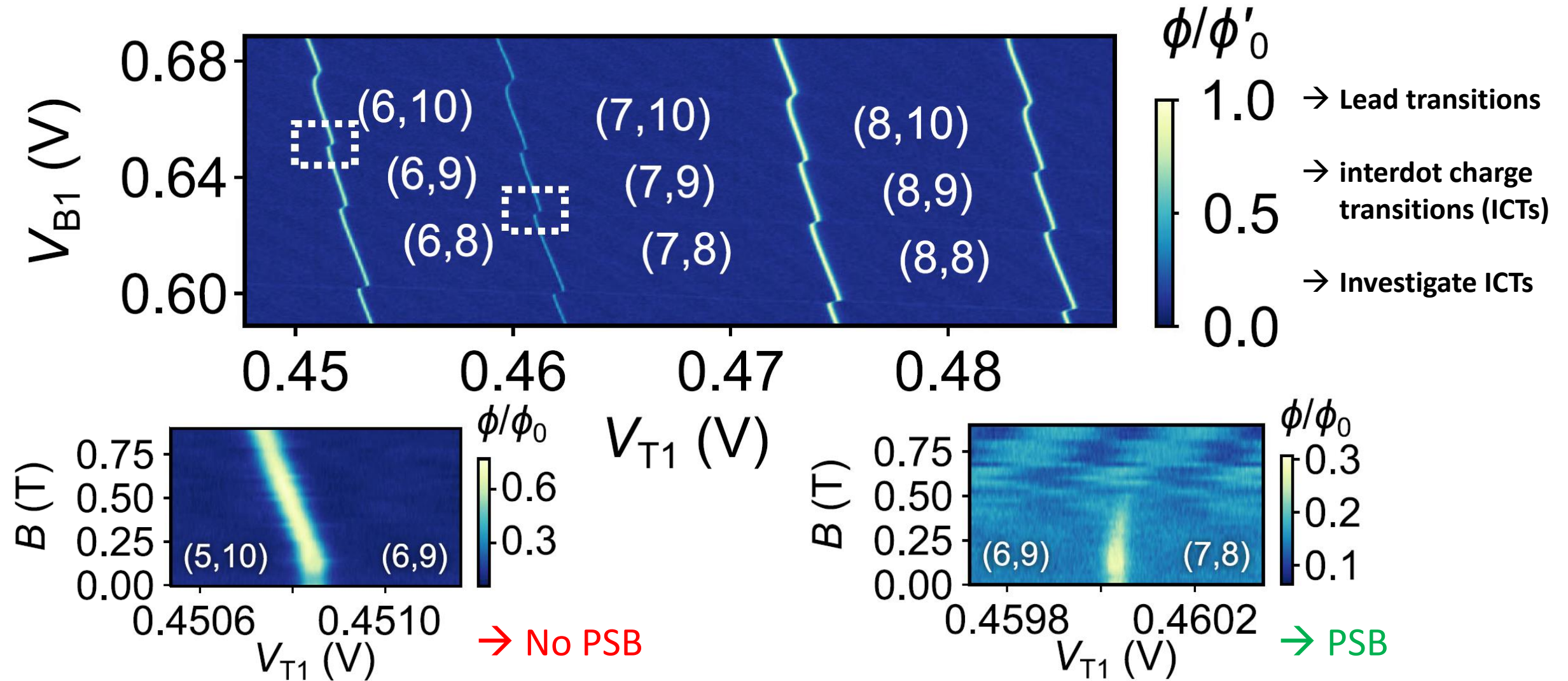
Recap: B-dependence at (0,2)-(1,1) transition

- Interdot charge transition (ICT)
 - Quantum capacitance $C_Q \propto \partial^2 E / \partial \epsilon^2$
 - Proportional to curvature of energy
 - At large enough B, a polarized triplet (T_{\pm}) becomes the ground state (no C_Q)
- Dispersively sensed ICT vanishes with B



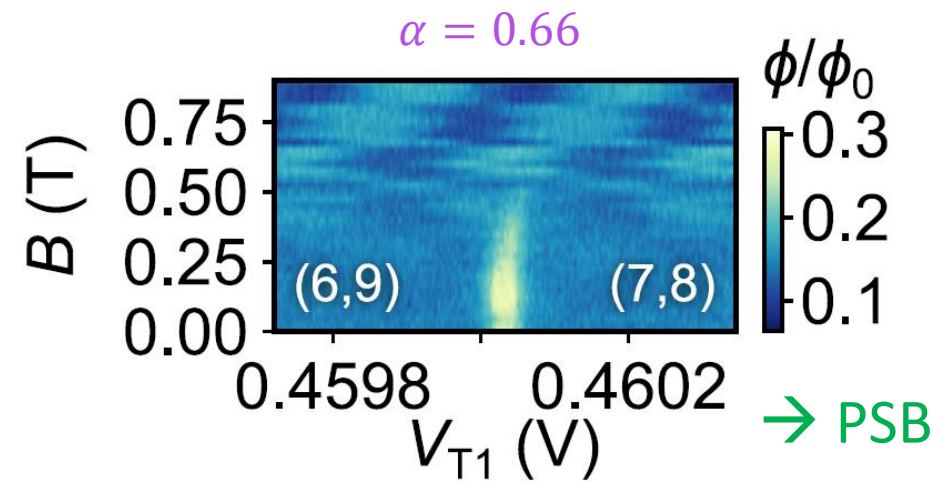
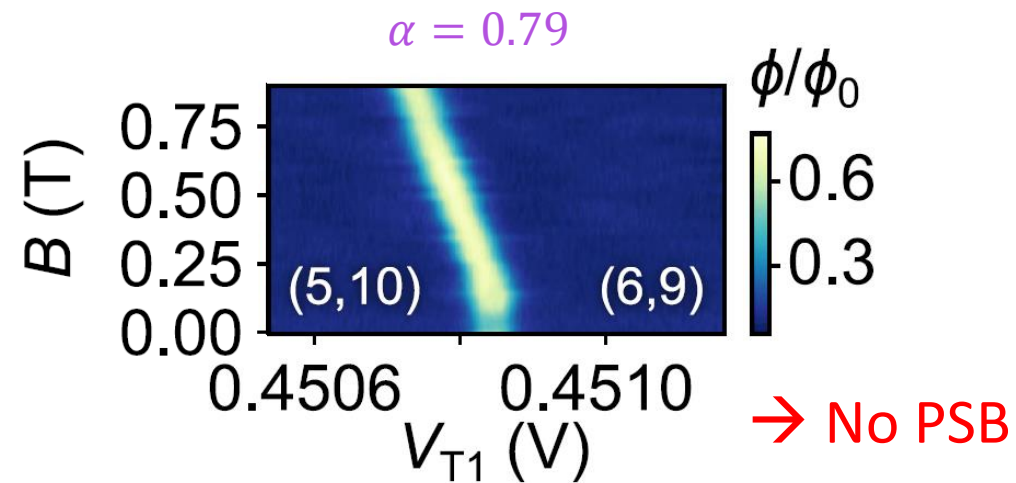
Crippa et al., Nature Comms. 2019

Detection of non-symmetric PSB



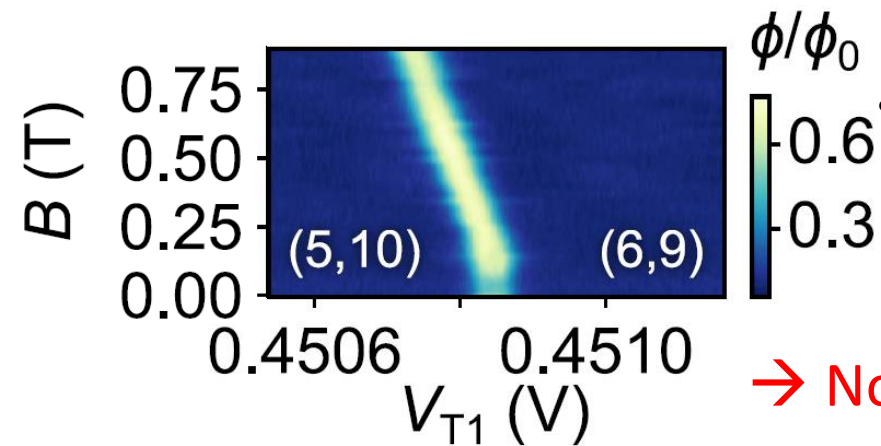
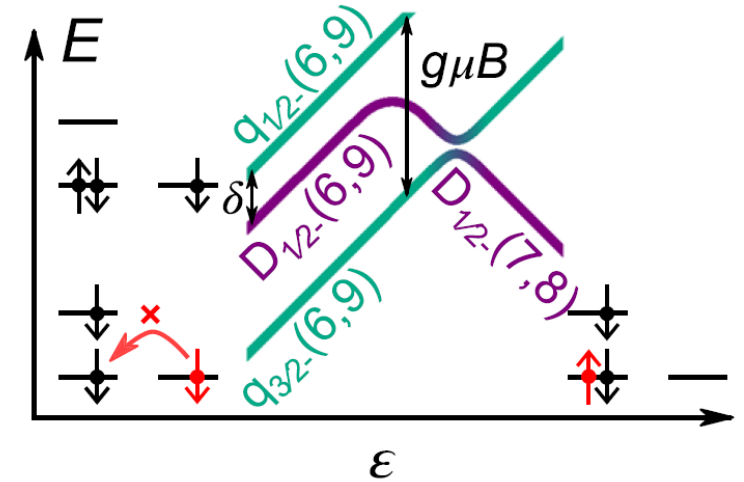
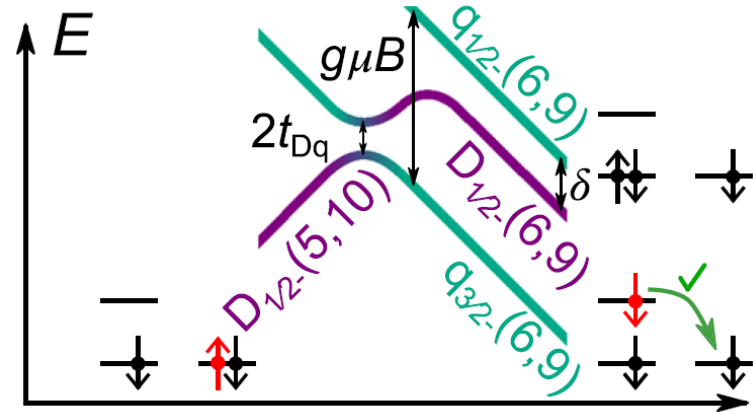
Detection of non-symmetric PSB

- Low $B \rightarrow$ cyclic tunneling between two states with same spin number due to resonator drive
- Increased $B \rightarrow$ Higher spin state becomes ground state
- If this state doesn't couple with the lower ones, system gets blocked (signal vanishes)
- Slopes of transitions (or vanishing thereof) can be used to deduce lever arm α (assuming $g=2$)



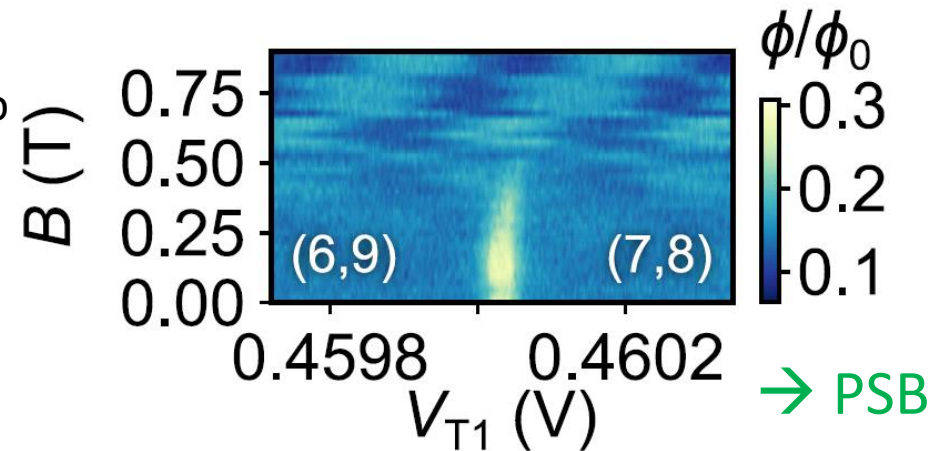
Detection of non-symmetric PSB

- Silicon QDs without spatial symmetries: First two full shells at $N=4,8$
- Doublets D with one unpaired electron ($S=1/2$)
- Quadruplets q with three unpaired electrons ($S=3/2$)
- B brings q(-3/2) down in E



→ No PSB

Left case: Hints at lifting due to spin-flip tunneling



→ PSB

Circuit QED analysis

Effective coherent DQD-resonator coupling between states i and j

Change in resonance frequency

$$f_r = f_0 - \frac{1}{2\pi} \frac{g_{\text{eff}}^2 \Delta_{ij}}{\Delta_{ij}^2 + \gamma_{ij}^2/4}$$

Change in effective linewidth

$$\kappa^*/(2\pi) = \kappa/(2\pi) + \frac{1}{2\pi} \frac{g_{\text{eff}}^2 \gamma_{ij}}{\Delta_{ij}^2 + \gamma_{ij}^2/4}$$

→ Expressions for f_r and κ^* can be fitted to the exp. to gain insight on t_{ij} and γ_{ij}

$$g_{\text{eff } ij}/(2\pi) = g_0/(2\pi) \langle i | \hat{n} | j \rangle$$

Coupling matrix element

Charge number operator

$$g_0/(2\pi) = \alpha f_0 \sqrt{Z_r/2R_Q}, \text{ with } \alpha = \text{const. assumed,}$$

Z_r : resonator impedance, R_Q : resistance quantum

t_{ij} : DQD tunnel coupling

$$\Omega_{ij} = \sqrt{\epsilon^2 + 4t_{ij}^2}$$

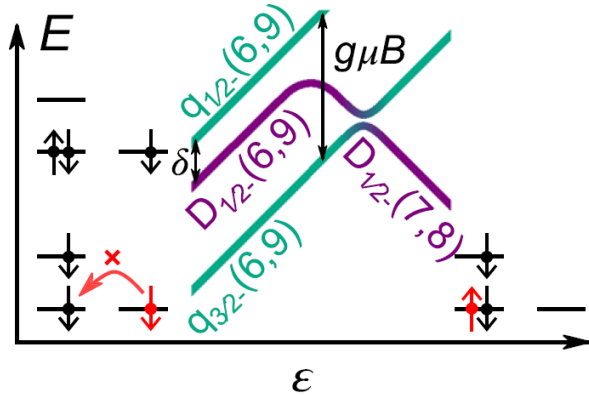
$$\Delta_{ij} = \Omega_{ij}/\hbar - 2\pi f_0$$

: energy diff. between participating states

κ : bare resonator linewidth

γ_{ij} : DQD decoherence rate

Circuit QED analysis: Case with PSB

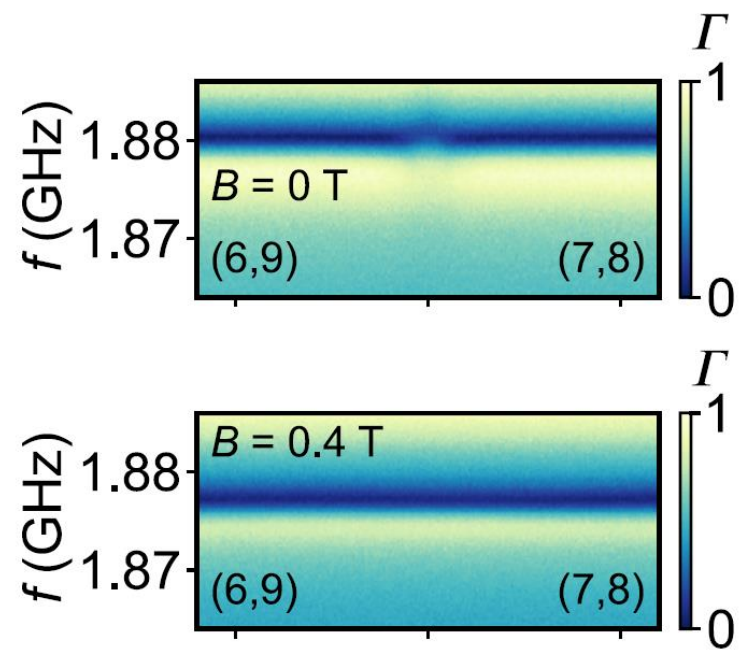


$$f_r = f_0 - \frac{1}{2\pi} \frac{g_{\text{eff}}^2 \Delta_{ij}}{\Delta_{ij}^2 + \gamma_{ij}^2/4}$$

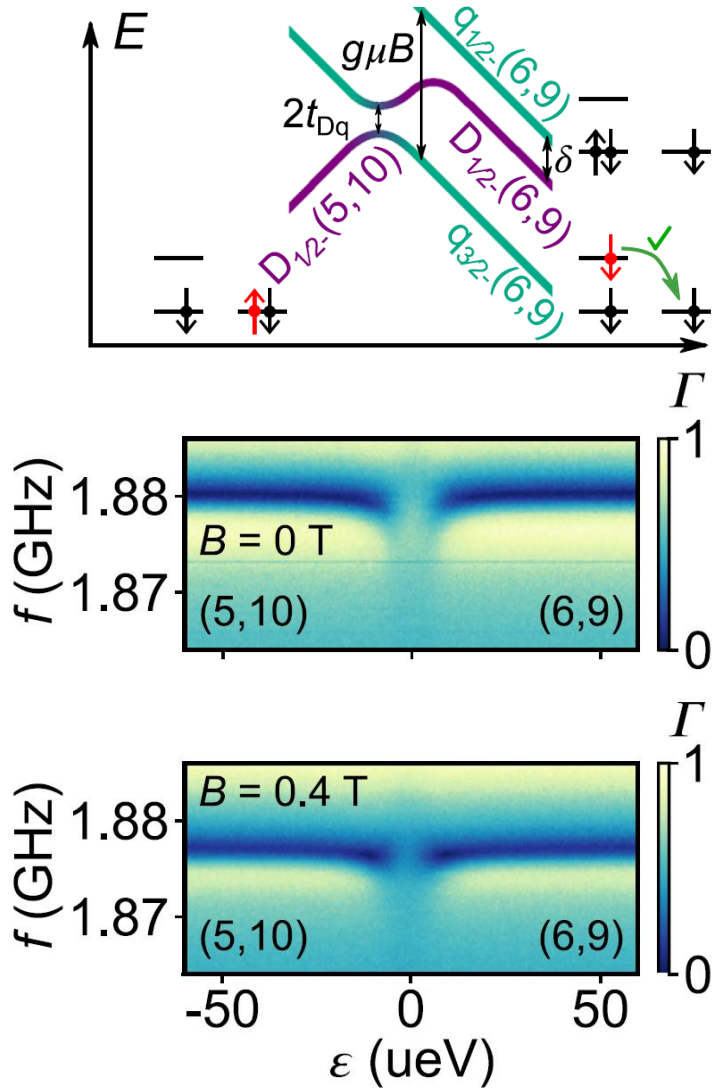
$$\Omega_{ij} = \sqrt{\varepsilon^2 + 4t_{ij}^2}$$

$$\Delta_{ij} = \Omega_{ij}/\hbar - 2\pi f_0$$

- B = 0T: f_R shifts upwards close to zero det. $\rightarrow g_{\text{eff}DD} > 0$ and $\Delta_{DD} < 0$
- So: $0 < 2t_{DD} < hf_0 = 7.8\mu\text{eV}$
- B = 0.4T: No changes to f_r , indicating $t_{Dq} \rightarrow 0$



Circuit QED analysis: Case without PSB

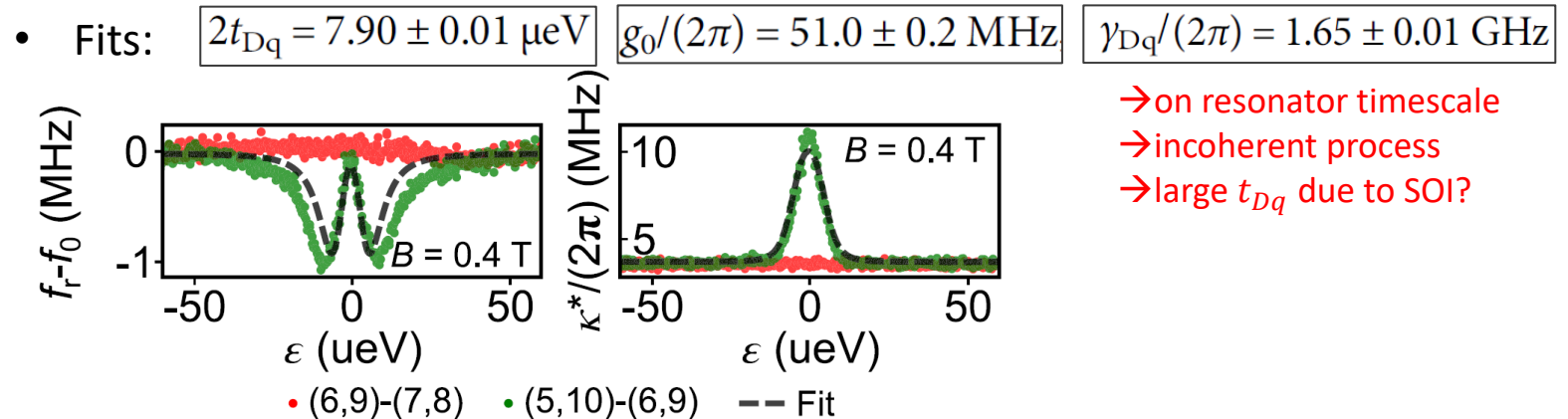


$$f_r = f_0 - \frac{1}{2\pi} \frac{g_{\text{eff}}^2 \Delta_{ij}}{\Delta_{ij}^2 + \gamma_{ij}^2/4}$$

$$\Omega_{ij} = \sqrt{\varepsilon^2 + 4t_{ij}^2}$$

$$\Delta_{ij} = \Omega_{ij}/\hbar - 2\pi f_0$$

- $B = 0\text{T}$: f_r shifts downwards close to zero det. $\rightarrow g_{\text{eff}DD} > 0$ and $\Delta_{DD} > 0$
- So: $2t_{DD} > hf_0 = 7.8\mu\text{eV}$ (remarkably large for electrons in Si)
- $B = 0.4\text{T}$: Changes to f_r remain substantial



Analysis for other ICTs

- Analysis done for 16 ICTs

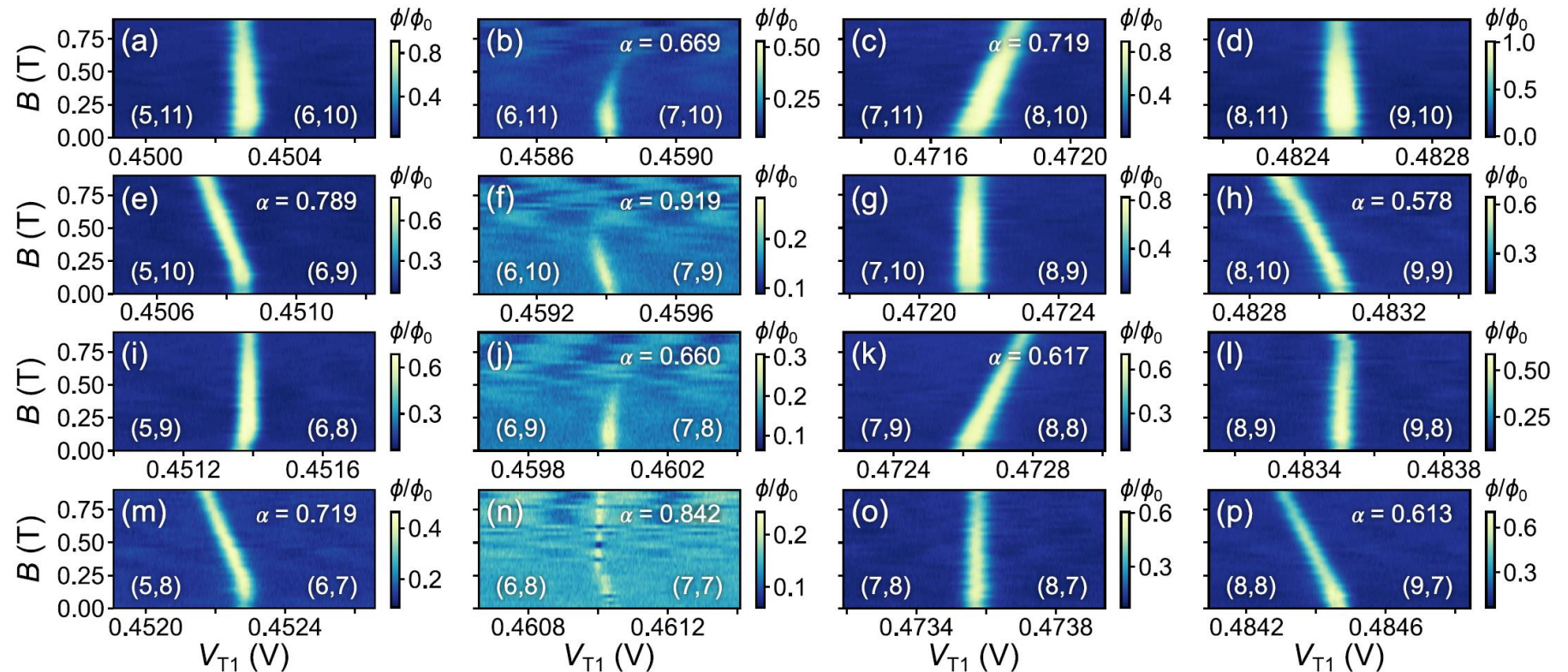
- 4 Categories identified:

→ lack of PSB (c,e,f,h,k,m,n,p)

→ PSB (b, j)

→ Obscured PSB (a,i) (large t_{ij})

→ Cases where spin GS remains same (d,g,l,o)



→ Periodicity of two in QD_{B1} (right index) occupancy indicates large level separation in 2nd QD

→ Consistently extracted $\langle \alpha \rangle = 0.7 \pm 0.1$ from transitions with slopes

Magneto spectroscopy simulations

Phase response is proportional to changes in the **parametric capacitance** $C_{pm} = (e\alpha)^2 \frac{\partial \langle n_2 \rangle}{\partial \varepsilon}$

e: electron charge, α : interdot lever arm, $\langle n_2 \rangle$: occupation probability of QD connected to resonator

$\langle n_2 \rangle$ can be expanded to: $\langle n_2 \rangle = \sum_i \langle n_2 \rangle_i P_i$ ← Occupation probability For each eigenstate i
← Polarization

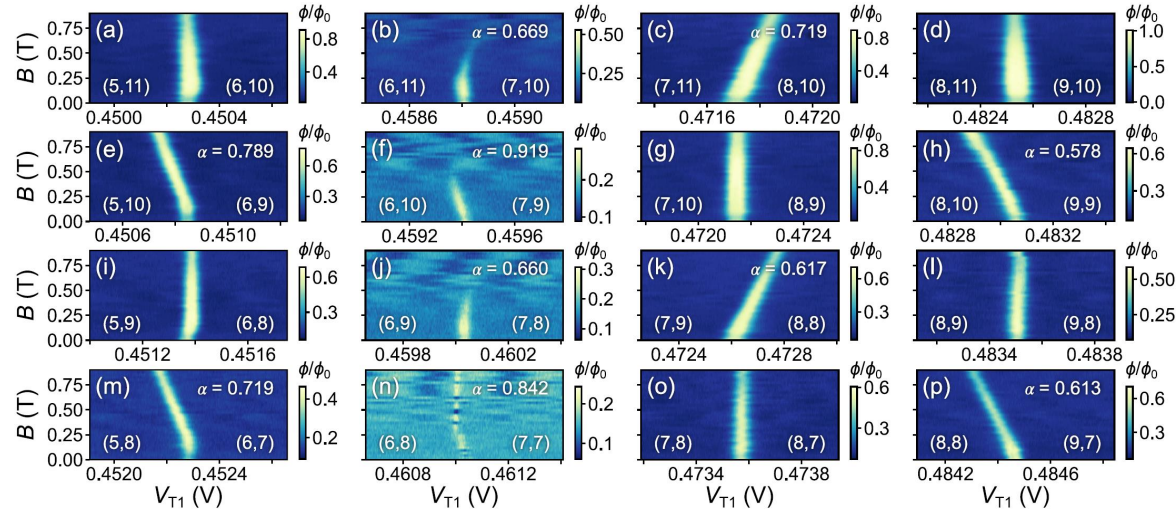
In this case, C_{pm} can be expanded to:

$$C_{pm} = (e\alpha)^2 \sum_i \underbrace{\frac{\partial \langle n_2 \rangle_i}{\partial \varepsilon}}_{\text{quantum}} P_i + \langle n_2 \rangle_i \underbrace{\frac{\partial P_i}{\partial \varepsilon}}_{\text{tunnelling}}$$

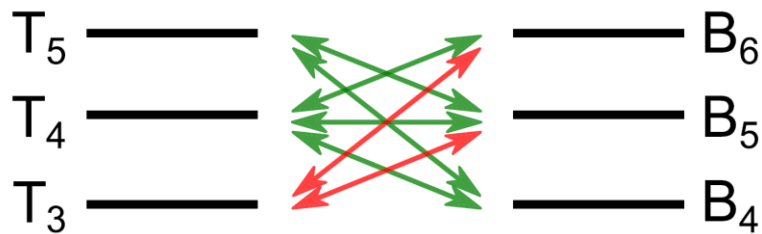
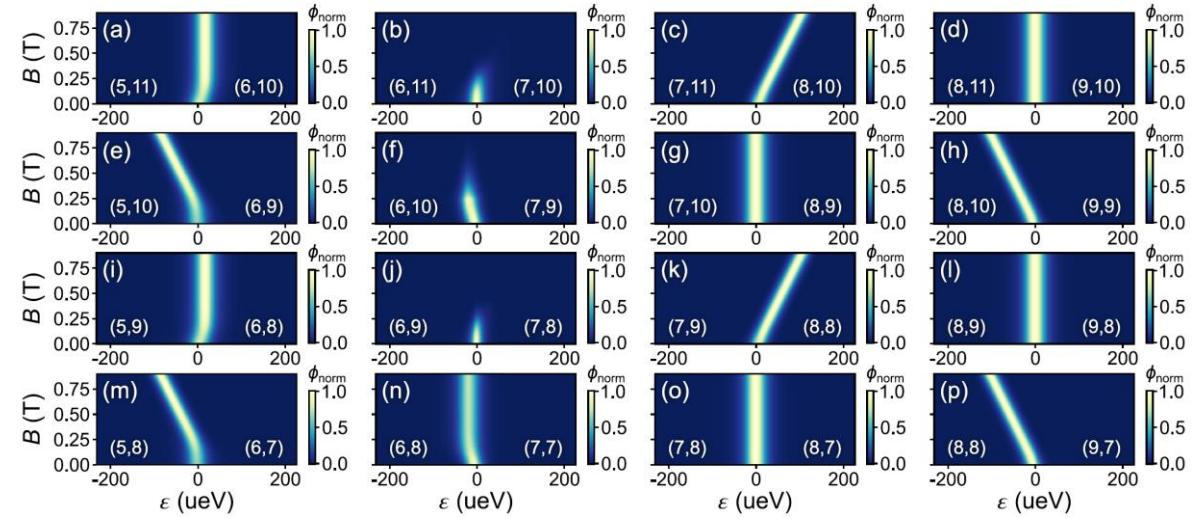
With $\langle n_2 \rangle_i = \frac{1}{2} \left(1 + 2 \frac{\partial E_i}{\partial \varepsilon} \right)$

Magneto spectroscopy simulations

Experiment



Simulations



transitions involving T_3 have **small t_{ij}**
and $\gamma_{ij} \ll f$
 \rightarrow PSB may only occur when B aligns
 with eigenvectors of combined g -
 tensor of DQD

- Dispersive magnetospectroscopy, and identification of energy spectra for 16 different ICTs
- Presence of non-symmetric PSB
- PSB lifting: High tunnel coupling $2t_{Dq} = 7.9\mu eV$, incoherent spin-flip process

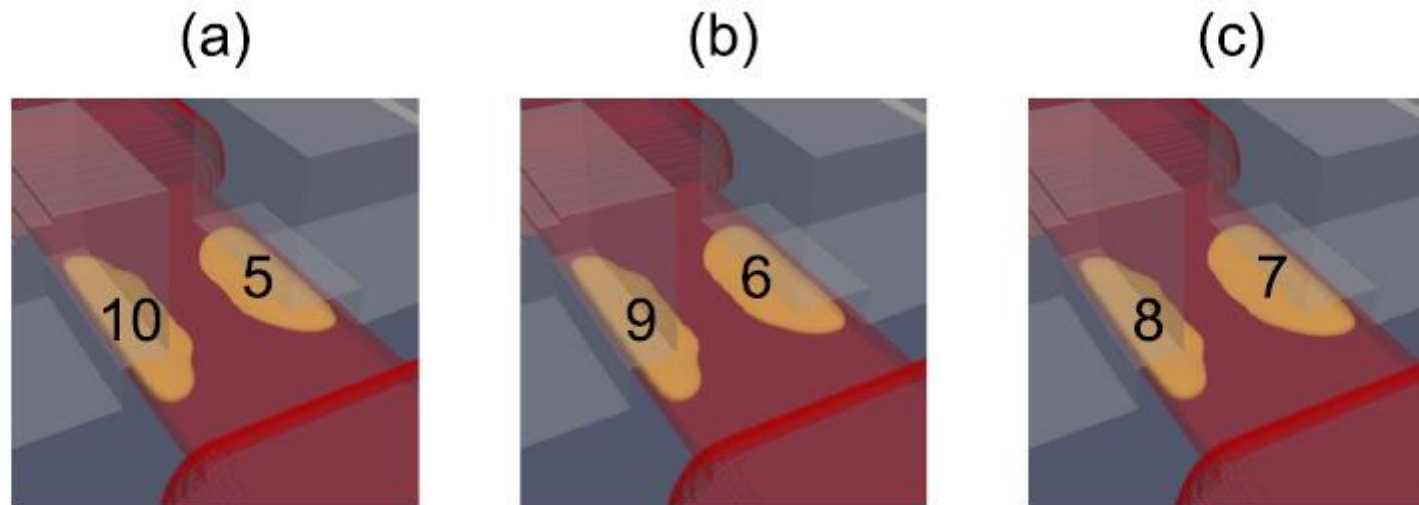


Fig. 5 | Simulation of the electronic density in the device in three electronic configurations totalling 15 electrons. The orange isosurfaces enclose 90% of the electrons. The red regions indicate the silicon nanowire and elevated source and

drain regions. The asymmetrically-placed split gates are represented in gray. Both the gate oxide and the Si_3N_4 spacers have been omitted for clarity. **a, b, c** Show the (5,10), (6,9), and (7,8) charge configurations, respectively.

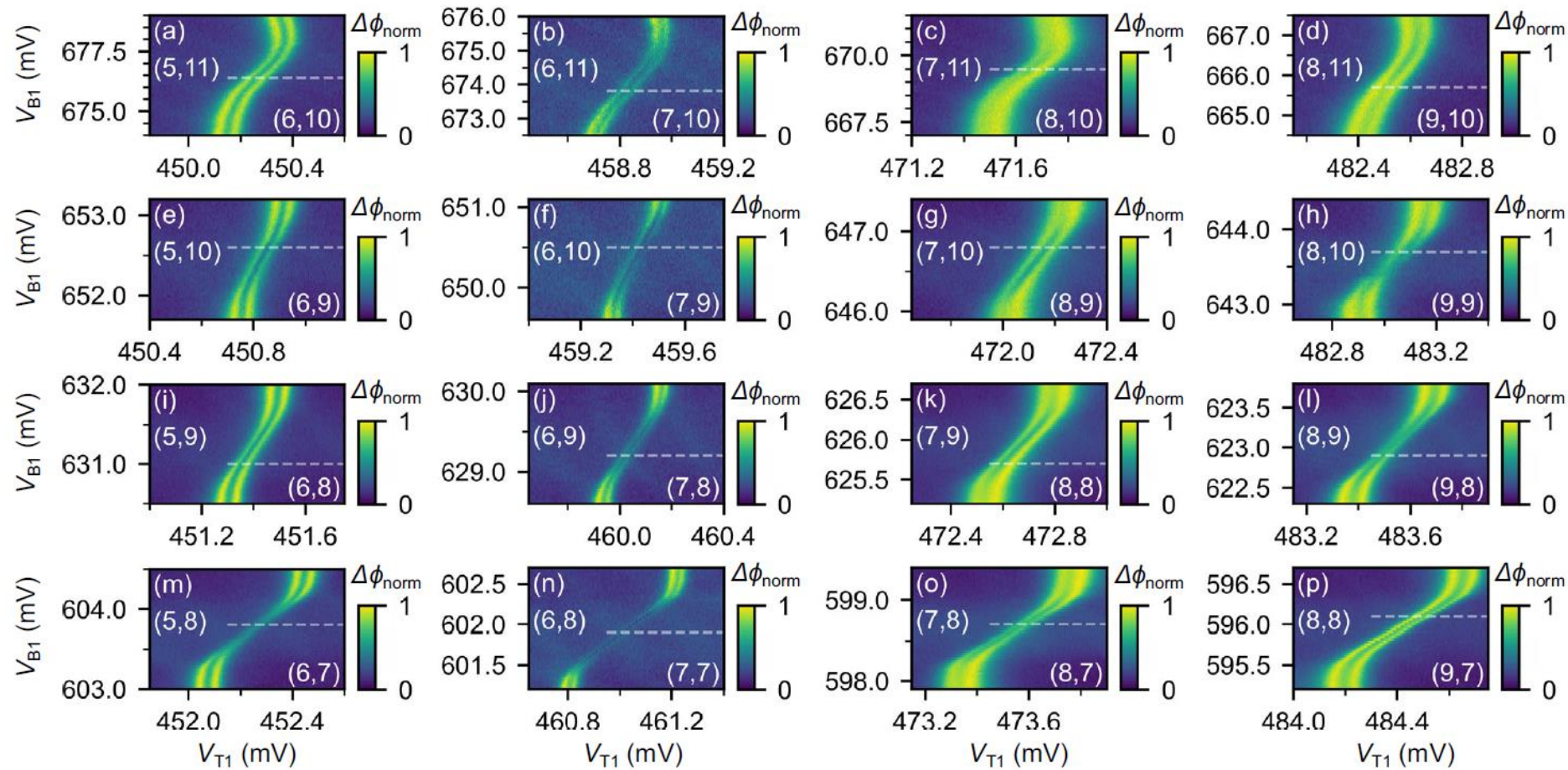


Fig. 6 | Zoomed-in charge stability diagrams of the 16 ICTs in Fig. 1(b).
a–p Measurement of the normalized phase shift $\Delta\phi_{\text{norm}}$ of the 16 ICTs visible in Fig. 1b. The numbers in parentheses indicate the electron occupancy of the DQD on

either side of the ICT and the dashed line indicates the V_{B1} used for the corresponding magnetospectroscopy measurements in Fig. 3. The double peak shape of the lines is a consequence of our choice of measurement frequency f .

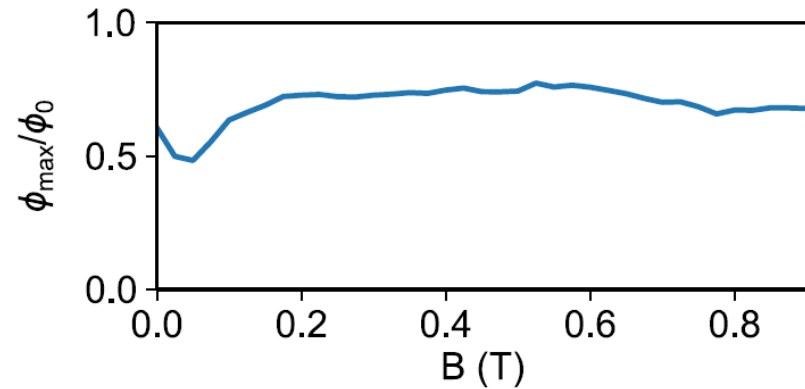


Fig. 7 | Maximum relative phase shift for each B -field linetrace of the magneto-spectroscopy measurement presented in Figs. 1d and 3e. The decrease in relative phase shift around $B = 45$ mT is due to a decrease in the resonator Q-factor at this magnetic field.

Description of fitting procedures

For the analysis of the resonator response as a function of detuning ϵ , we use the steady-state power reflection coefficient developed from the Heisenberg-Langevin equations of motion in its complex Lorentzian form³⁷

$$|S_{11}| = \left| 1 - \frac{i\kappa_{\text{ext}}/(2\pi)}{f - f_r + \frac{i}{2}\kappa^*/(2\pi)} \right|^2 \quad (3)$$

where $\kappa_{\text{ext}}/(2\pi) = 1.76$ MHz is the external photon decay rate, and where f_r , as well as $\kappa^*/(2\pi)$ are defined in Eqs. (1) and (2) in the main text. To obtain the values for f_r and $\kappa^*/(2\pi)$ plotted in Fig. 2g, h as well as Fig. 9a, b below, we fit each ϵ line trace of the data presented in Fig. 2c–f to Eq. (3).

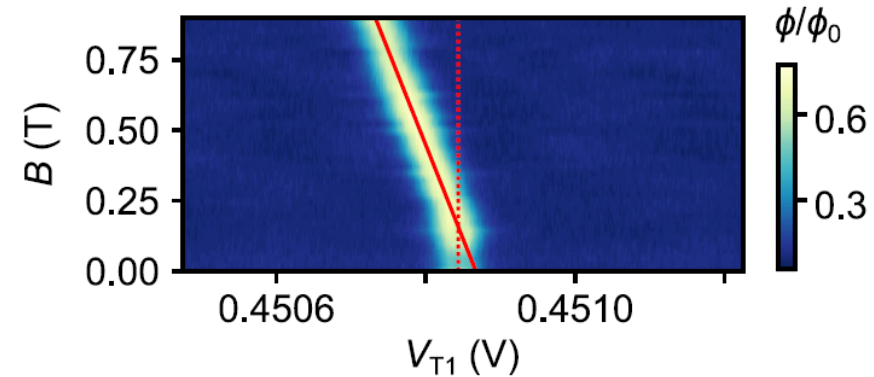


Fig. 8 | Measurement of the relative phase shift of the (5,10)–(6,9) ICT as a function of magnetic field B . The dotted red line marks the central position of the phase shift signal at $B = 0$ T, whereas the solid red line fits the sloped region for $B > 0.2$ T and is extrapolated to $B = 0$ T.

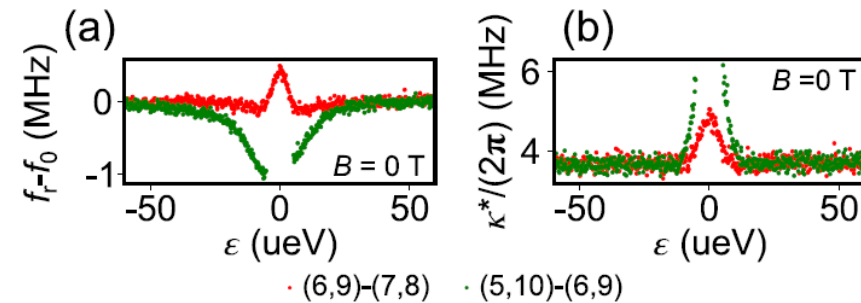


Fig. 9 | Resonator-double quantum dot interaction. **a, b** Resonance frequency f_r and effective linewidth κ^* as a function of ϵ for ICTs (6,9)–(7,8) [red] and (5,10)–(6,9) [green] at $B = 0$ T determined by Lorentzian fits to the data in Fig. 2c, d.

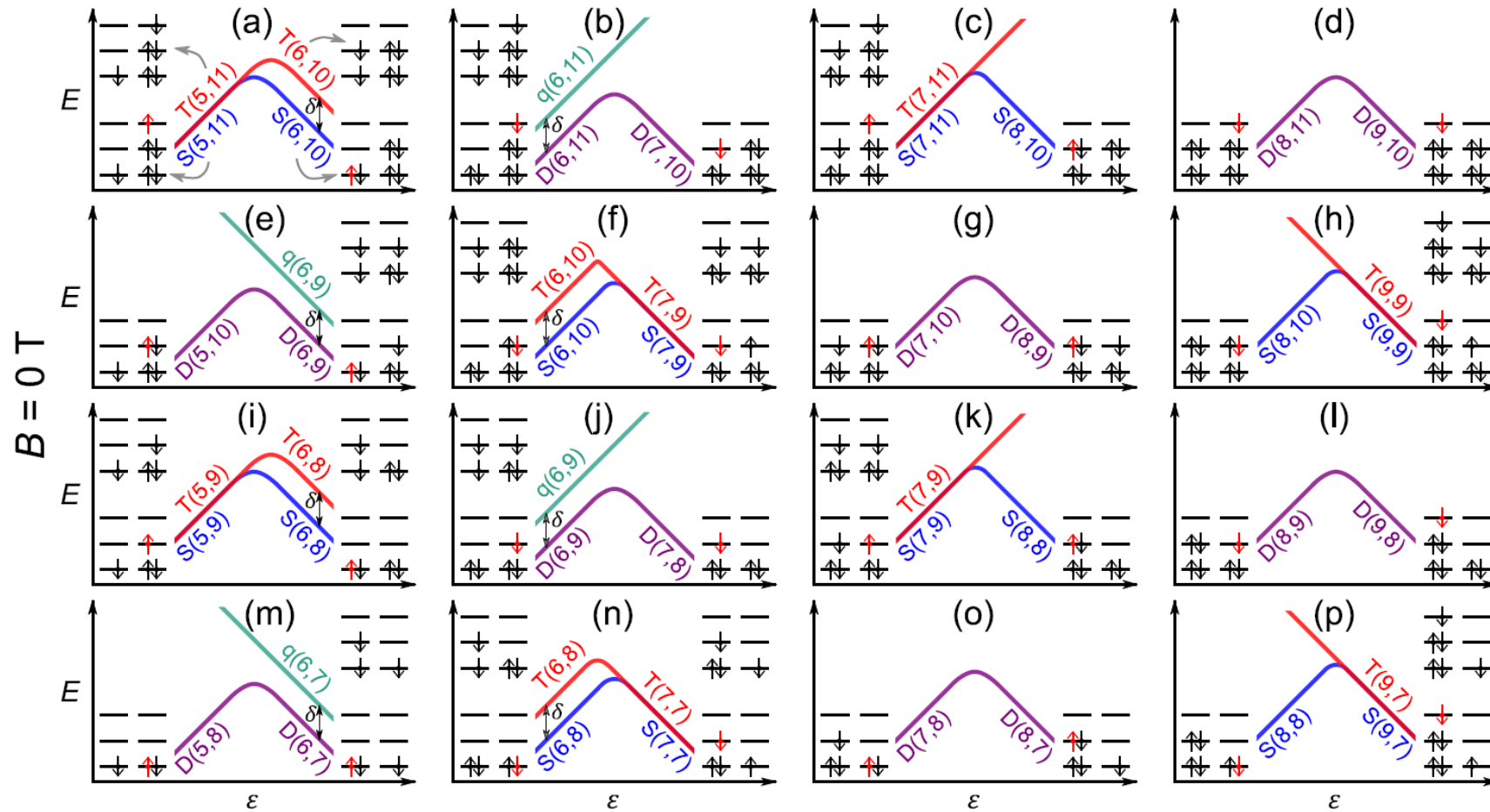


Fig. 10 | Energy spectra at $B = 0$ T. a–p Illustrative single-particle and DQD energy levels as a function of detuning ϵ at $B = 0$ T for the charge states involved in the 16 ICTs present in the charge stability diagram of Fig. 1b. For simplicity, the single-particle energy levels omit the two (three) lowest-lying energy levels of QD_{T1}

(QD_{B1}), such that the six energy levels shown are $T_3, T_4, T_5, B_4, B_5, B_6$ starting from the bottom left. The red electron indicates the electron that moves QD as a function of changes in ϵ .

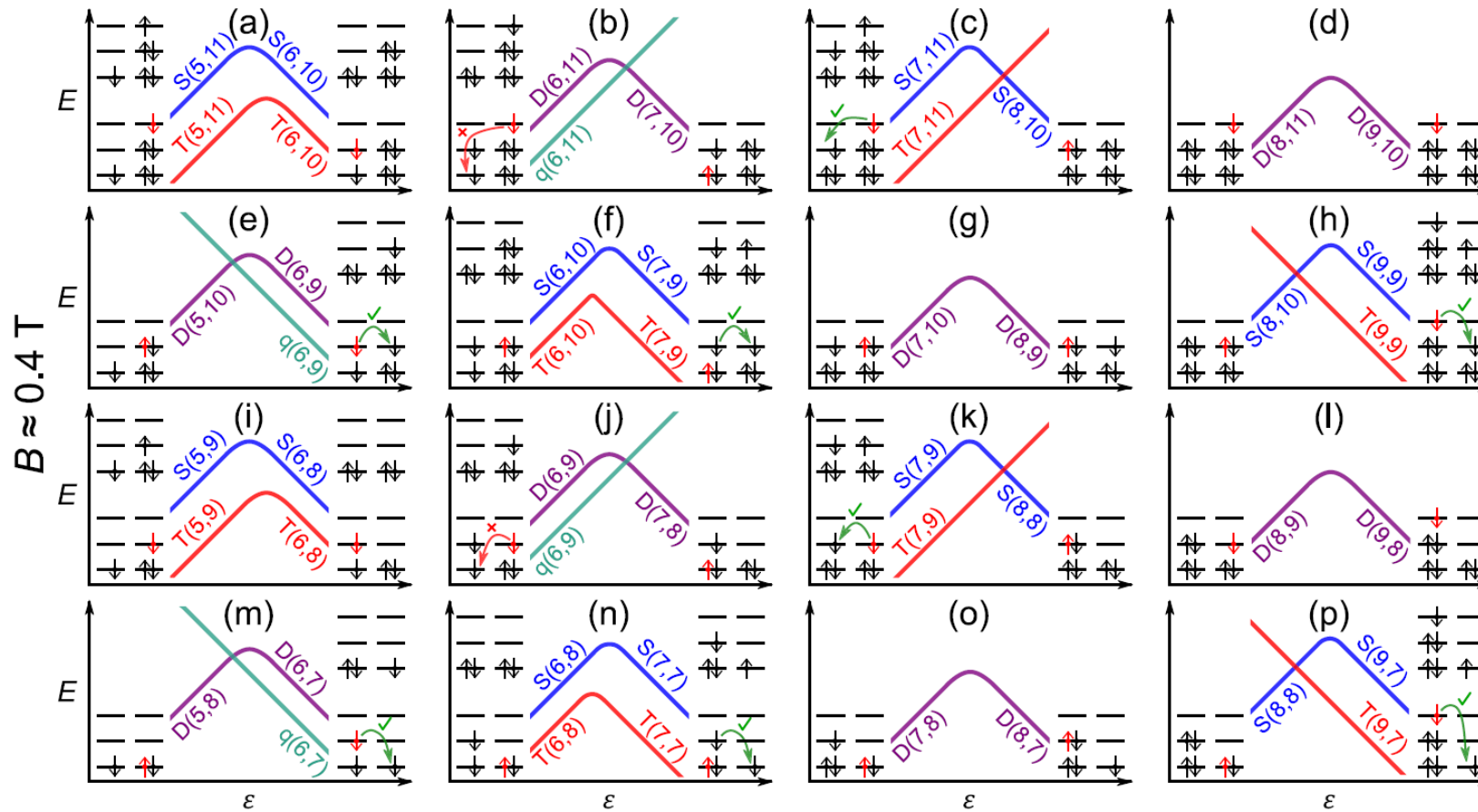


Fig. 11 | Energy spectra at $B = 0.4$ T. a–p Illustrative single-particle and DQD energy levels as a function of detuning ϵ at $B = 0.4$ T for the charge states involved in the 16 ICTs present in the charge stability diagram of Fig. 1b. For simplicity, the single-particle energy levels omit the two (three) lowest-lying energy levels of QD_{T1} (QD_{B1}), such that the six energy levels shown are $T_3, T_4, T_5, B_4, B_5, B_6$ starting from

the bottom left. The red electron indicates the electron that moves QD as a function of changes in detuning, and the green (red) arrows indicate (the lack of) spin-flip tunneling. Note that the green arrows in (f, n) indicate spin-flip tunneling in the singlet–triplet manifold, which happens only when $B \lesssim \delta/(g\mu_B) = 0.16$ T.

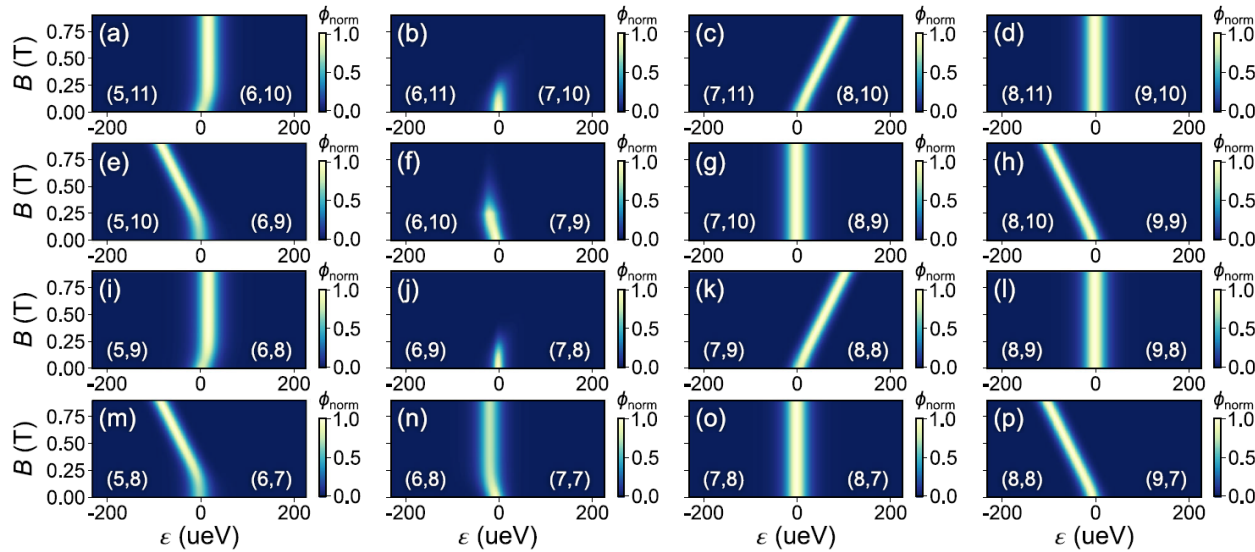


Fig. 12 | Magnetospectroscopy simulations of the 16 studied ICTs. a–p Qualitative simulation of the normalized phase shift of each ICT visible in Fig. 1b and their energy spectra in Figs. 10, 11 as a function of B using the parameters in Table 1. The numbers in parentheses indicate the electron occupancy of the DQD on either side of the ICT.

Table 1 | Parameters used to perform qualitative magnetospectroscopy simulations shown in Fig. 12 for the energy levels shown in Figs. 10 and 11

Panel	$2t_S$ or $2t_D$ (μeV)	$2t_T$ or $2t_q$ (μeV)	δ_N (μeV)	δ_P (μeV)	Relaxation regime
a	20	20	0	18	Slow
b	15	20	18	>120	Slow
c	10	20	0	>120	Fast
d	20	20	>120	>120	Fast
e	20	20	>120	18	Fast
f	10	3	18	0	Fast
g	20	20	>120	>120	Fast
h	10	20	>120	0	Fast
i	20	20	0	18	Slow
j	7	20	18	>120	Slow
k	10	20	0	>120	Fast
l	20	20	>120	>120	Fast
m	20	20	>120	18	Fast
n	10	20	18	0	Fast
o	20	20	>120	>120	Fast
p	10	20	>120	0	Fast

Columns two through five list the magnitude of the needed energy spectrum parameters, and the last column indicates whether the simulations consider the slow or fast relaxation regime. All simulations use $T = 80$ mK.